JOURNAL OF GEOPHYSICAL RESEARCH, VOL. 113, D00E03, doi:10.1029/2008JD010054, 2008

Ground-based infrared retrievals of optical depth, effective radius, and composition of airborne mineral dust above the Sahel

D. D. Turner[1]

Received 2 March 2008; revised 30 September 2008; accepted 29 October 2008; published 19 December 2008.

[1] Mineral dust aerosol optical depth (AOD) at 11 μm and effective radius are retrieved from ground-based spectral infrared (8–13 μm) radiance observations collected in Niamey, Niger, in 2006 with the Atmospheric Radiation Measurement (ARM) mobile facility. The algorithm used in this study has the ability to differentiate between two different mineral types, allowing the AOD and effective radius of each mineral to be retrieved as long as the minerals have significant and spectrally different absorption bands in the infrared. Kaolinite, gypsum, and quartz, common minerals found in African deserts, have different infrared absorption features and are used in this work. The mineral combination that yielded the best fit to the observations, after accounting for the increased degrees of freedom in the dual mineral fits, was identified as the "radiatively significant" composition of the dust. The results were analyzed as function of period (premonsoon, early monsoon, late monsoon, and postmonsoon) as well as by back-trajectory direction. High-AOD events occurred in all four periods, with more high-AOD events occurring during the drier premonsoon and postmonsoon periods. Kaolinite is an important component to the dust, with 94% of the retrievals having a significant amount of this mineral. Kaolinite + gypsum was determined to fit the spectral observations the best in nearly two thirds of the observations. Additionally, the amount of gypsum was dependent on the back-trajectory direction, with a larger fraction of the total AOD due to gypsum when the flow was from east of the Niamey site.

Citation: Turner, D. D. (2008), Ground-based infrared retrievals of optical depth, effective radius, and composition of airborne mineral dust above the Sahel, *J. Geophys. Res.*, *113*, D00E03, doi:10.1029/2008JD010054.

1. Introduction

[2] Climate change, and in particular anthropogenic climate change predicted by numerical models, is arguably one of the more important issues facing scientists and policymakers today. However, in order to characterize and quantify anthropogenic climate change, many components of the climate system need to be better understood. In particular, aerosol radiative forcing is very uncertain in climate models [*Schwartz and Andreae*, 1996]. Mineral dust composes a significant fraction of the atmospheric aerosol, yet the total radiative forcing due to dust can be either positive or negative at the top of the atmosphere owing to a large number of factors such as the size distribution of the dust particles, the optical depth of the dust, the surface albedo, etc. [*Tegen et al.*, 1996]. Additionally, aerosol forcing in the infrared is generally not included in many climate models, even though atmospheric dust can have a large impact on the infrared radiative fluxes at the surface and top of the atmosphere [*Vogelmann et al.*, 2003].

[3] Mineral dust in the atmosphere is often episodic, and particular atmospheric conditions are needed to loft the dust from the Earth's surface into the atmosphere [e.g., *Washington et al.*, 2006a, 2006b]. Atmospheric dust can impact surface temperatures [*Tegen et al.*, 2006], and owing to the radiative heating in the column, dust can also modify the circulation of the atmosphere [*Tegen et al.*, 1996]. Thus, the impact of dust on climate is very uncertain [*Intergovernmental Panel on Climate Change*, 2001].

[4] Atmospheric dust is primarily composed of clay minerals and silicates [*Falkovich et al.*, 2001], but the exact composition depends on a multitude of factors including the parent surface, the process that mobilized the dust initially, and the atmospheric conditions that are keeping the dust aloft [*Sokolik and Toon*, 1999]. Atmospheric dust must be traced back to its source region and the optical properties and chemical composition characterized in order to improve dust emission and transport models [*Kinne et al.*, 2003].

[5] A variety of investigators have attempted to retrieve the composition of mineral dust from ground-based remote sensors. *Dubovik et al.* [2000, 2002] have developed a method to retrieve the refractive index of atmospheric dust from AERONET sunphotometer data [*Holben et al.*, 1998]; however, this method has significant uncertainties when the visible optical depth is low (i.e., below approximately 0.15). *Kassianov et al.* [2005] used solar direct and diffuse observations from a multifilter rotating shadowband radi-

---

[1] Space Science and Engineering Center, University of Wisconsin-Madison, Madison, Wisconsin, USA.

0148-0227/08/2008JD010054

ometer (MFRSR) to derive the refractive index and particle size of dust aerosols, but their method fails when the aerosol particles are too large. *Koven and Fung* [2006] investigated the differences in dust optical properties in the visible and near infrared over North Africa. Dust composition has also been inferred from space-borne MISR observations [*Kalashnikova et al.*, 2005]. All of these techniques used radiance or irradiance observations in the visible or near-infrared mainly to characterize the amount of hematite in the dust, as hematite has an absorption band in the visible portion of the spectrum.

[6] In this study, we use spectrally resolved zenith infrared radiance (8–13 μm) data to determine the composition of the airborne dust, as well as the optical depth and effective radius of the dust particles. *Rathke et al.* [2002] were able to identify the "radiatively significant" aerosol composition using spectrally resolved infrared observations in Antarctica to surmise the chemical composition of the aerosol. As Rathke et al. point out, we can only surmise what the true composition of the mineral dust is, because some aerosol chemical species do not have spectral signatures in the 8- to 13-μm band (e.g., hematite has no spectral features in the imaginary refractive index in this band [*Marra et al.*, 2005]), while other minerals may have similar refractive index spectra (e.g., kaolinite and montmorillonite [*Roush et al.*, 1991]). Hence, we will restrict our analysis to quartz, gypsum, and kaolinite minerals, as these are among the main constituents in atmospheric dust [*Sokolik and Toon*, 1999], and these three minerals also have distinctly different absorption bands in the infrared (Figure 1). The refractive indices of these three minerals result in unique ground-based infrared radiance spectra (Figure 2), from which the composition of the mineral can be deduced. However, like Rathke et al., our results will only yield the "radiatively significant" composition of the mineral dust, because the infrared will have no sensitivity to some minerals that do not have infrared absorption bands and will be unable to determine between minerals that have very similar absorption bands.

[7] Knowledge of the mineral dust composition is not only important for the validation of aerosol transport models, but also for properly characterizing the radiative impact of the dust. Figure 3 illustrates the differences in the top-of-atmosphere (TOA) and surface longwave radiative fluxes as a function of the mineral aerosol optical depth (AOD) for kaolinite, gypsum, and quartz. These calculations, computed using the line-by-line discrete ordinates (LBLDIS) radiative transfer model [*Turner*, 2005], used temperature and water vapor profiles measured by a radiosonde launched at the Niamey site on 15 March 2006 that had a precipitable water vapor amount of 1.36 cm (typical premonsoon conditions). A single dust layer was assumed to exist in the lowest 1 km of atmosphere, and the effective radii of the dust particles as specified to be 1.5 μm. The differences in the downwelling longwave radiation at the surface are approximately 10 W/m^2 for large AOD values among the three different compositions. However, the differences in TOA longwave flux at large AOD approach 15 W/m^2, with a kaolinite dust layer yielding significantly larger TOA flux values than dust layers composed of either of the other two minerals. This difference in TOA sensitivity is explained by the location of the absorption bands of the different minerals, with the primary absorption band for kaolinite overlapping with the 9.6-μm ozone band, which thus mutes the affect of the kaolinite dust particles on the TOA flux. The sensitivity of the longwave radiative flux to the mineral composition is thus quite significant, implying that studies that investigate the connection between the radiative properties of dust and the structure of the lower troposphere must account for the composition of the dust particles.

[8] We have analyzed the one year of data collected in 2006 by the Atmospheric Emitted Radiance Interferometer (AERI), which is part of the Atmospheric Radiation Measurement (ARM) program's mobile facility (AMF). The AMF was deployed to Niamey, Niger (2.18°E, 13.48°N; Figure 4) as part of the Radiative Atmospheric Divergence using AMF, GERB (Geostationary Earth Radiation Budget experiment), and AMMA (African Monsoon Multidisciplinary Analysis) Stations (RADAGAST) experiment; details of this experiment including motivation, background, and general synoptic conditions is given by *Slingo et al.* [2008]. For cases where no clouds were overhead, the optical depth, effective radius, and the radiatively significant mineral composition were retrieved from the high-spectral-resolution infrared radiance observations made by the AERI. These data were then analyzed to look at the distribution of optical depth, effective radius, and composition as a function of season and wind direction to characterize the dust properties above the Niamey site. While the data set does not span a long enough time period to develop a robust climatology of the dust, these results are useful for gaining insight into the properties of the dust above Niamey, for analyzing the radiative impact of the dust, for aerosol emission/transport model validation, and for satellite validation.

2. Instrumentation

[9] The AMF started operation in Niamey on 7 January 2006 and collected data until 6 Jan 2007 with a wide variety of in situ and remote sensing instrumentation, including state-of-the-art passive radiometers [*Miller and Slingo*, 2007]. In addition to the AERI (described in detail below), this analysis also uses data from the microwave radiometer (MWR) and radiosonde profiles to characterize the atmospheric state, which is needed in the retrieval process (described in section 3).

[10] Vaisala RS92 radiosondes were launched every 6 h during the RADAGAST campaign; however, these radiosondes have a daytime dry bias and perhaps a small nighttime bias as well [*Cady-Pereira et al.*, 2008; *Vömel et al.*, 2007]. We have scaled the radiosonde humidity profile using a height-independent scale factor that removes, to first order, the bias in the humidity profile [*Turner et al.*, 2003]. This scale factor is the ratio of the precipitable water vapor retrieved from the MWR [*Turner et al.*, 2007] to the integrated water vapor from the original radiosonde profile; thus, the scaled radiosonde humidity profile is now consistent with the MWR-retrieved PWV value. This process significantly reduces the variability in the calibration of the radiosonde humidity profiles and accounts for any bias in the PWV in the radiosonde data [*Turner et al.*, 2003].

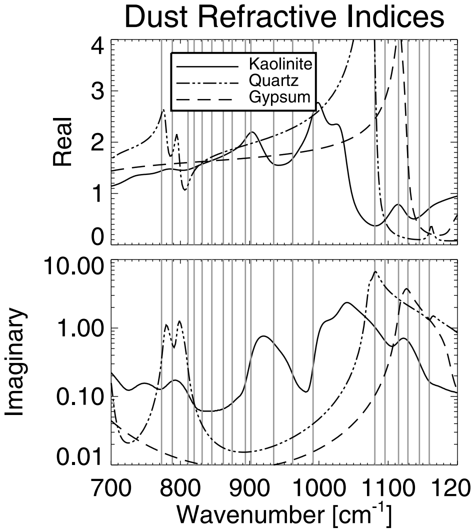

Figure 1. Refractive indices of kaolinite [*Roush et al.*, 1991], gypsum [*Aronson et al.*, 1983], and quartz [*Spitzer and Kleinman*, 1961] in the thermal infrared. The vertical gray bars are the locations of the 19 microwindows used in the retrieval (from Table 1).

2.1. AERI: Basic Information

[11] Developed for the ARM program, the AERI is an automated infrared interferometer that measures downwelling radiation from 530 to 3050 cm^{-1} (19.0 to 3.3 μm) with 1 cm^{-1} resolution [*Knuteson et al.*, 2004a, 2004b]. The AERI is built around a commercial interferometer and uses mercury cadmium telluride (MCT) and indium antimonide (InSb) detectors in a "sandwich" arrangement that provide good sensitivity to downwelling infrared radiation. The field-of-view of the instrument is 46 mrad. The AERI periodically views two well-characterized, high-emissivity blackbodies, one of which is held at 60°C while the other floats at ambient temperature. During RADAGAST, the AERI measured downwelling radiance from the atmosphere for 3 min, and then looked at each of the blackbody targets for approximately 2 min, resulting in a complete measurement cycle of about 7 min per sky spectrum with excellent signal-to-noise ratio across the spectrum.

[12] The dust retrieval algorithm assumes that the instrument has good radiometric calibration. The absolute calibration of the radiance data is better than 1% of the ambient radiance (3-σ) and is achieved through accurate monitoring of the blackbody temperatures (as well as the structural temperatures around the blackbodies) together with corrections for the instrument self-apodization and nonlinearity in the MCT detector [*Knuteson et al.*, 2004b]. The radiometric uncertainty of the AERI observations is determined from the imaginary portion of the calibration equation [*Knuteson et al.*, 2004b], and thus the scene-dependent instrument noise is determined directly for each AERI observation. AERI data have been used to evaluate and improve radiative transfer models, inverted to retrieve profiles of temperature and humidity, and to retrieve cloud properties in ice-only, liquid-only, and mixed-phase clouds.

[13] An important feature of all ARM AERI systems, including the system deployed to Niamey, is that the front end of the optical system, i.e., where the scene-selection mirror and blackbodies are located, is enclosed and a ventilating fan is used to direct air upward out of the AERI's sky port. The incoming air is filtered to remove any particles, and the outgoing airflow keeps atmospheric dust from settling on the scene mirror. If large particles, such as dust, were present on the gold scene mirror then this would effectively broaden the AERI's field-of-view (FOV) via scattering, and thus it may be possible for the FOV to fall outside the aperture of the blackbodies and/or sky port. To mitigate this possibility, a baffle with an aperture is fitted to the scene mirror. This baffle rotates with the scene mirror, thus ensuring that if the FOV is indeed being broadened by the presence of dust on the scene mirror that the contribution from outside the normal FOV comes from this baffle. This contribution would then be the same for both the blackbody and sky views, and thus the contribution would be removed via the calibration process [*Knuteson et al.*, 2004a].

2.2. AERI: Correction for Warm Bias

[14] While the AERI blackbodies are well characterized and corrections are applied to account for the nonlinearity of the longwave detector, we have observed a very small warm bias in the radiance observations from multiple AERI systems relative to line-by-line radiative transfer model

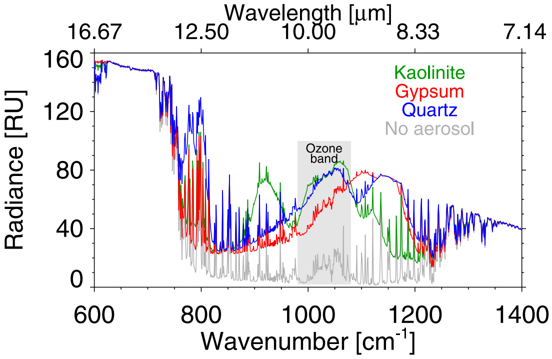

Figure 2. Downwelling radiance at the surface for four different simulations: an aerosol-free case and three cases with an aerosol layer composed of minerals of a single composition. In the aerosol cases, the AOD was set to 1.0 at 900 cm^{-1}, the effective radius was 1.4 μm, and the aerosol layer existed from the surface to 1 km. The thermodynamic profile is from a radiosonde observation on 7 March 2006 at Niamey, and the PWV is 1.06 cm. The kaolinite aerosol case has a larger radiance signal at 920 cm^{-1} relative to the other two mineral calculations, the gypsum has a larger radiance signal at 1100 cm^{-1}, and quartz has larger radiance at 780 cm^{-1}. These spectral differences in the downwelling radiance allow the mineral composition to be determined from the AERI radiance observations. Note that the 9.6-μm ozone band, which covers the spectral region from approximately 980 to 1080 cm^{-1}, is highlighted here because there are significant uncertainties in the ozone concentration that make using data in this spectral region problematic for aerosol retrievals. A "radiance unit" (RU) is 1 mW/(m^2 sr cm^{-1}).

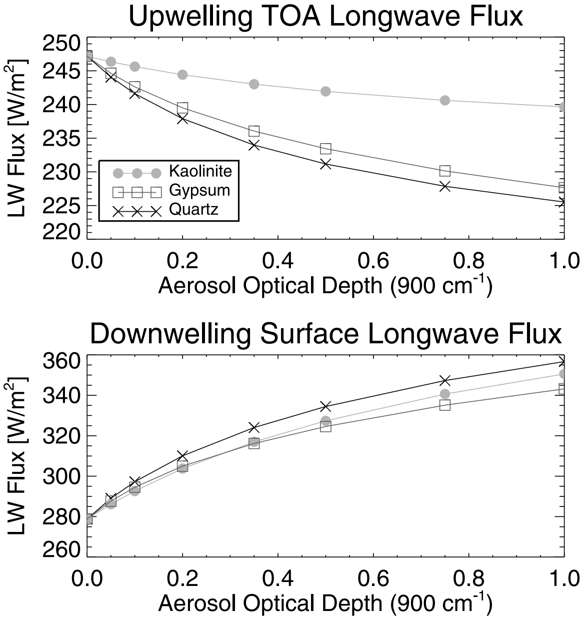

Figure 3. Sensitivity of the computed top-of-atmosphere (TOA) and surface longwave radiative flux to mineral dust composition as a function of 11-μm AOD for an atmosphere typical of premonsoon conditions over Niamey, Niger, that has a single dust layer near the surface.

calculations (even in cases with a pristine scene mirror). This warm bias, which is approximately 1 mW/(m^2 sr cm^{-1}), is most easily identifiable in clear-sky conditions with very low amounts of PWV. This bias has been observed in several different AERI data sets, including the systems at the ARM Southern Great Plains site [*Turner et al.*, 2004], the ARM North Slope of Alaska site (J. S. Delamere et al., A far-infrared radiative closure study in the Arctic: Application to water vapor, manuscript in preparation, 2008), and for the AERI data set collected during the Surface Heat Energy Budget of the Arctic (SHEBA) campaign [*Turner*, 2003]. *Turner* [2003] demonstrated that this bias is not associated with the model calculations (e.g., errors in the input water vapor profile, model parameters such as water vapor continuum). Our hypothesis is that the warm bias is due to a small contribution inside the instrument that is not accounted for in the instrument's calibration; however, this bias appears to be constant over time for each particular instrument. Following *Turner* [2003], we model this bias as if there were a slight obstruction in the instrument's field-of-view,

$$N_{obs} = f\ B\left(T_{eff}\right) + (1 - f)N_{sky}, \qquad (1)$$

where the observed radiance is given by N_{obs}, the true sky (scene) radiance by N_{sky}, the fraction of the field of view filled by the obstruction is given by f, the emissivity of the obstruction is assumed to be 1, and the effective temperature of the obstruction (T_{eff}) is assumed to be the temperature of the support structure of the instrument (which is observed and stored in the data). The fraction f is assumed to be independent of wavelength, while all of the other terms have wavelength dependence.

[15] To determine the value of f using equation (1), we need to have a good estimate of N_{sky}, which we compute using the line-by-line radiative transfer model. The uncertainty in calculation of N_{sky} is reduced if there are no aerosols to be accounted for and the water vapor amount is small. Thus, we searched for dust-free cases with low PWV near a radiosonde launch time in our data set. An initial analysis of the retrievals (described below) suggested that these conditions existed on 2 May, 2 November, and 23–26 December 2006 (9 cases). Using the line-by-line radiative transfer model calculation (which used the MWR-scaled radiosonde profiles as input) as the true clear-sky radiance N_{sky}, the values of f were derived using radiance in the 830–840 cm^{-1} region (note that gypsum, quartz, or kaolinite have an absorption band here). The mean value of f from these nine cases is 0.010 ± 0.002. Because the AERI was not moved after its initial setup, obstruction fraction f was assumed to be constant for the entire year, and the data were corrected by rearranging equation (1) to compute N_{sky} from the AERI observation N_{obs}.

[16] The application of the obstruction correction reduces the magnitude of the observed radiance spectra slightly, thus reducing/eliminating the warm bias in the AERI observations. Correcting for the warm bias results in a mean reduction in the retrieved AOD of approximately 0.05 relative to the original radiance observations.

3. Retrieval Algorithm

[17] A retrieval algorithm, called the MIXed-phase Cloud Retrieval Algorithm (MIXCRA), was used to retrieve the AOD and effective radius of the mineral dust. This algorithm was developed initially to retrieve the optical depth and effective radius of both the liquid and ice components simultaneously in mixed-phase clouds from AERI radiance observations [*Turner*, 2005] by taking advantage of the different absorption bands of liquid and ice to separate the two phases (ice is more absorbing than liquid at 12 μm

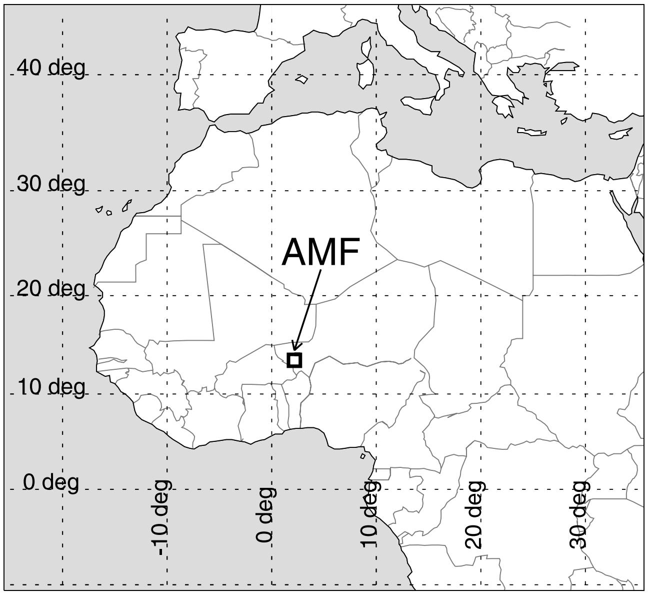

Figure 4. AMF location in Africa.

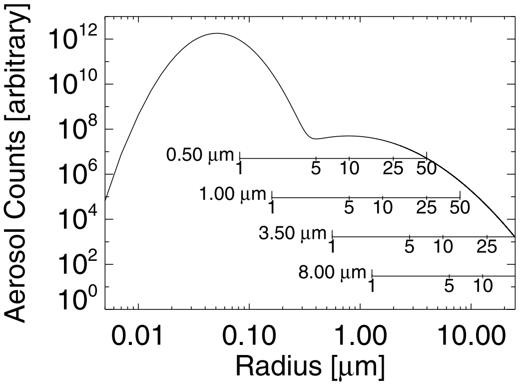

Figure 5. Arbitrary bimodal aerosol size distribution, with the size parameters for various wavelengths (0.5, 1.0, 3.5, and 8.0 μm) indicated with the horizontal bars.

while the opposite is true at 18 μm). In order to separate the optical depth of any two components (e.g., liquid versus ice, ice versus dust, different types of dust) using this algorithm, the refractive indices must be "orthogonal" (i.e., not correlated with wavelength). Simply stated, there must be spectral regions where one mineral is more absorbing than the other and vice versa in the spectral range spanned by the AERI observations and in spectral bands that are not opaque at the surface (such as the 15-μm CO_2 band, or 6.7-μm water vapor band). For this reason, the contribution to the AOD of minerals that have no spectral absorption features cannot determined, nor can the relative contributions between two minerals with similar refractive indices be separated; this is why this method is only able to determine the "radiatively significant" composition.

[18] The setup and mechanics of the aerosol retrieval performed here are similar to the approach used by *Turner* [2005]. We have replaced the scattering properties look-up tables of *Turner* [2005] with tables that are appropriate for the kaolinite, gypsum, and quartz particles (details are below). The retrieval algorithm uses an optimal estimation approach; therefore the optical depth of one "phase" can be essentially fixed to zero using the a priori input forcing the algorithm to become a single-mineral retrieval, if desired. The state vector **X** is defined as $\mathbf{X} = [\tau, r_e]$ for a single-mineral retrieval or $\mathbf{X} = [\tau_1, r_{e1}, \tau_2, r_{e2}]$ when a dual-mineral retrieval is performed (the subscripts 1 and 2 indicate different minerals), where τ is the AOD for the mineral and r_e is the corresponding effective radius. The a priori state vector, which is utilized by the optimal estimation retrieval, is assumed to have $\tau = 0.3 \pm 0.5$ and $r_e = 0.8 \pm 0.3$ μm for each mineral. The Jacobian matrix, which captures the sensitivity of the forward model to perturbations in the state vector, is estimated using finite differences of the LBLDIS calculations.

[19] Simulated radiance observations with realistic random noise were used to evaluate the accuracy of the retrieval algorithm. The results (which are similar to the mixed-phase cloud results of *Turner* [2005]) demonstrate that the algorithm is able to determine the total AOD very accurately (within 1%), but that there is a small amount of "cross talk" in separating the relative amount of AOD for each mineral (in a dual-mineral retrieval); this error is less than 5%.

[20] There are many free parameters in the aerosol retrieval problem that either need to be assumed or retrieved. For example, the aerosol size distribution is typically bimodal (as illustrated in Figure 5), with a fine and a coarse mode, and the chemical composition of each mode can be different. These two modes are typically modeled as lognormal distributions, but the mean value and the width of the two modes can be quite variable and depend strongly on the composition, source region, and aging of the aerosol particles. However, the thermal infrared observations are primarily sensitive to only the coarse mode of the aerosols, as indicated by the 8.0-μm bar in Figure 5 which shows the size parameter ($\chi = 2\pi r/\lambda$) as a function of the aerosol radius. For $\chi \ll 1$ the aerosol particles are in the Rayleigh scattering regime and the emission contribution to the downwelling radiance is negligible; consequentially the 8- to 13-μm AERI observations are essentially insensitive to the fine mode aerosols. In should be noted that both the fine and the coarse modes must be accounted for when computing the dust's contribution to the shortwave radiant flux.

[21] Thus, we have chosen to model the dust as a single-mode lognormal size distribution, where the width of the size distribution was assumed to be 0.7 μm and the mean value of the distribution is allowed to change to provide a range of effective radii from 0.01 to 12 μm. (The MIXCRA retrievals are relatively insensitive to this assumed spectral width value.) Even though there is significant evidence to the contrary, we assume that the dust particles are spherical so that Mie theory can be used to compute the single scattering properties of the dust particles from the refractive indices. *Kalashnikova et al.* [2005] concluded that errors in the assumed shape of the dust particles were unlikely to impact their retrievals significantly even though their radiance observations were in the visible and near-IR wavelengths where scattering is a much larger signal than the aerosol emission. Our assumption of spherical particles will not impact the accuracy of our infrared retrievals significantly since the dust absorption is quite high and the retrieval is based upon the emission of the dust particles. We also assume an external mixture of the dust composition (i.e., that each dust particle is composed of a single mineral but that there are particles of different minerals within the volume); this may introduce some small errors in the retrieved variables. There is evidence that clay minerals, even "nonswelling" clays such as kaolinite, can adsorb water vapor and thus swell to larger sizes and change the scattering properties of the aerosol [*Schuttlefield et al.*, 2007]; however, since this water vapor uptake is a strong function on the exact nature of the mineral sample, we assume no dependence on relative humidity here. Finally, *Dufresne et al.* [2002] have demonstrated that scattering effects in the longwave are not insignificant and need to be accounted for; because the radiative transfer model used in MIXCRA is LBLDIS, a combination of the line-by-line radiative transfer model LBLRTM and discrete ordinates radiative transfer solver DISORT [*Turner*, 2005], scattering is accounted for in our retrieval.

[22] Since gypsum, kaolinite, and quartz all have significantly different absorption bands in the 8- to 13-μm region (Figures 1 and 2), the MIXCRA algorithm was used to separate the total AOD signal into components of any two of these minerals simultaneously. However, in a dual-

Table 1. Wavelength Regions Used in MIXCRA Retrieval of Mineral Dust[a]

Starting Wave number (cm^{-1})	Ending Wave number (cm^{-1})	Center Wavelength (μm)
770.9	774.8	12.94
785.9	790.7	12.69
809.0	812.9	12.33
815.3	824.4	12.20
828.3	834.6	12.03
842.8	848.1	11.83
860.1	864.0	11.60
872.2	877.5	11.43
891.9	895.8	11.19
898.2	905.4	11.09
929.6	939.7	10.70
959.9	964.3	10.39
985.0	998.0	10.09
1076.6	1084.8	9.25
1092.1	1098.8	9.13
1113.3	1116.6	8.97
1124.4	1132.6	8.86
1142.2	1148.0	8.73
1155.2	1163.4	8.63

[a] These spectral regions are chosen in “microwindows” in the spectrum that are relatively free of water vapor or other gaseous absorption lines. No microwindows were used in the 980–1080 cm^{-1} region owing to the strong ozone contribution to the radiance in this spectral region.

mineral retrieval, the algorithm attempts to fit the observed radiance with 4 separate variables (τ_1, τ_2, $r_{e,1}$, and $r_{e,2}$, where 1 and 2 refer to minerals 1 and 2 used in the retrieval, respectively, τ is the optical depth, and r_e is the effective radius), while there are only 2 degrees of freedom if the algorithm is run in single-mineral mode (i.e., solving for τ_1 and $r_{e,1}$ because τ_2 is assumed to be zero). However, because of the additional degrees of freedom, the dual-mineral retrieval will always result in a better fit to the observed radiance than if the algorithm were run in a single-mineral mode, but it may not be a statistically better fit. Thus, MIXCRA was run 6 separate times for each cloud-free AERI observation: three times in single-mineral mode (kaolinite-only, gypsum-only, quartz-only) and three times in dual-mineral mode (kaolinite + gypsum, kaolinite + quartz, gypsum + quartz). For the converged retrieval in each of the six cases, the root-mean square difference between the observed radiance and the computed radiance in the 19 microwindows used in the retrieval (Table 1) was computed, and the compositions that yielded the best single-mineral fit and dual-mineral fit for each sample were identified. (A microwindow is a region of the spectrum between absorption lines.) A statistical F test was then applied to determine if the best dual-mineral fit was indeed statistically better than the best single-mineral fit; the best fit retrieval (whether single or dual mineral) was saved for that AERI observation.

[23] Finally, while there is information on the vertical distribution of the aerosols above Niamey from the AMF micropulse lidar, the lidar is sensitive primarily to the vertical distribution of the fine mode aerosols because it operates at a wavelength of 0.523 μm. Thus, we have assumed that the mineral dust is a homogeneous layer (i.e., has constant infrared extinction) from the surface to 1.5 km. The assumed constant extinction profile may result in a small error in the effective radiating temperature of the dust layer that translates into an error in the retrieved optical depth; however, the impact is relatively small for optical depths less than 1. In the retrievals performed here, we have assumed that the uncertainty in the effective temperature of the dust layer is 2 K, and this translates into an uncertainty of less than 0.02 in the retrieved AOD. A small error in the effective temperature of the layer (i.e., the vertical profile of the dust extinction) does not affect either the retrieved effective radius or composition.

4. Results

[24] The MIXCRA retrievals were applied to all of the cloud-free AERI observations during the AMF deployment to Niamey, as radiance from clouds (even thin cirrus) would affect the ability of the algorithm to determine the mineral composition of the dust. The micropulse lidar data and the temporal variability of the AERI radiance at 11 μm were used to identify cloudy periods and eliminate them from the analysis; nonetheless, a large number of samples (16,755) were analyzed since a large fraction of the yearlong data set was cloud-free. We first will illustrate the aerosol retrieval algorithm’s capability on a 4-day period in March when a significant dust storm event occurred in the Sahel. Then, the results from the year-long analysis will be presented and discussed.

4.1. Case Study: Dust Storm Event

[25] From 7 to 10 March 2006, the Niamey area experienced a widespread dust storm event that was triggered by an anomalously strong northerly flow, which lofted and carried large amounts of dust from and through northern and central Africa. *Slingo et al.* [2006] described this storm and its impact on both the longwave and shortwave radiative fluxes at the surface and top-of-the-atmosphere. The mineral dust properties were retrieved from the AERI data during the cloud-free periods during this event.

[26] Figure 6 provides some example AERI radiance observations during this dust storm (blue), along with LBLDIS calculations using both the MIXCRA-retrieved aerosol properties (red) and assuming no aerosols (i.e., “clear” or pristine sky conditions in gray). In each of the four cases, the kaolinite + gypsum retrieval was determined to be the best mineral combination, with the 11-μm AOD of the kaolinite and gypsum given by τ_1 and τ_2, respectively. (All AOD values are henceforth at 11 μm unless otherwise noted.) The results in Figure 6 illustrate the quality of the fit across the 8- to 13-μm spectrum, including matching the spectral features at 920 cm^{-1} and 1120 cm^{-1}, for both the prestorm example on 7 March at 0334 UTC (τ_{tot} = 0.12) and the three examples from the dust storm (τ_{tot} = 0.59, 0.51, and 0.69, respectively). Interestingly, the kaolinite fraction, defined here as $F_{kao} = \tau_{kao}/\tau_{tot}$ where τ_{kao} is the AOD of the kaolinite, changed significantly as the dust storm evolved (from F_{kao} = 65–68% on the 7 and 8 March to F_{kao} = 43% on 10 March), with the winds on 7 March and 8 March being from the north while the winds on 10 March were more easterly (see section 4.2 for more discussion regarding the dependence of F_{kao} on wind direction). The difference between the AERI observation

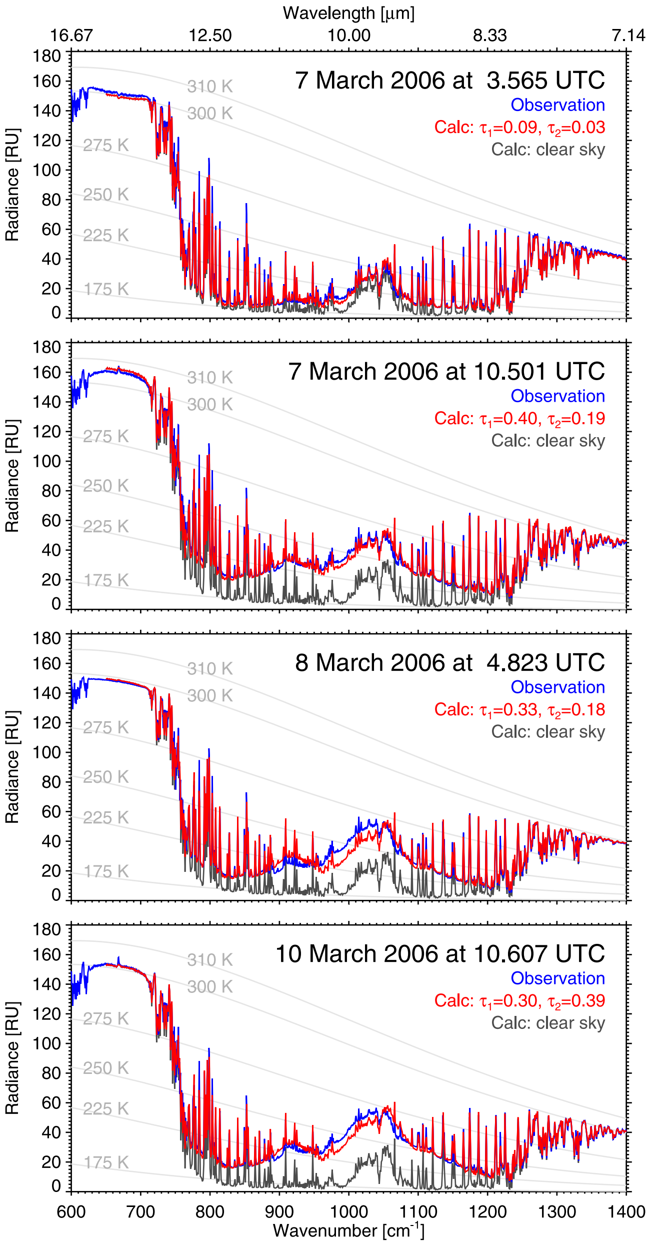

Figure 6. AERI-observed infrared downwelling radiance (blue), LBLDIS computed radiance where the input dust properties were retrieved from the observations by MIXCRA (red), and aerosol-free radiance calculations (gray) for 4 different cloud-free times during the March 2006 dust storm. The retrieved 11-μm AODs for kaolinite and gypsum are given by τ_1 and τ_2, respectively. A "radiance unit" (RU) is 1 mW/(m^2 sr cm^{-1}).

and the "clear-sky" calculation indicates the spectral radiance signature of the dust forcing at the surface. It should be noted that ozone is a major contribution to the downwelling radiance from 980 to 1080 cm^{-1}, and the MIXCRA algorithm does not use any information in this spectral region in the retrieval owing to the uncertainty in the ozone concentration with height above the instrument. The agreement between the AERI radiance observations and the LBLDIS calculation in 980–1080 cm^{-1} spectral region is fortuitous since the ozone concentration and the temperature profile in the middle-to-upper stratosphere was unknown.

[27] Most ground-based aerosol remote sensing techniques use observations in the visible or near-infrared (i.e., wavelengths shorter than 1.05 μm), and consequentially are limited to daytime conditions only. The AERI-based aerosol retrievals do not have this restriction, and thus the variability of the AOD across the diurnal cycle can be investigated. Figure 7 shows the evolution of the 11-μm AOD (blue) for this 4-day period, as well as the derived effective radius (red) from the MIXCRA retrievals. Figure 7 also shows the 1.02-μm AOD retrievals from the AERONET Cimel sunphotometer [*Dubovik et al.*, 2000] (purple crosses), located at the rural Banizoumbou site 60 km east of Niamey, where the Cimel data have been scaled by log(11.0 μm/1.02 μm). The AOD at 0.5 μm retrieved from the MFRSR [*Kassianov et al.*, 2005] at the AMF site is also shown (green diamonds). During this 4-day period, optically thin cirrus appeared overhead for several short intervals; these periods were identified by analysis of the micropulse lidar data and are indicated by the gray shaded vertical bars. The MIXCRA retrievals were performed in these cloudy periods for this case study to illustrate the impact that optically thin clouds have on the retrieved dust properties. Note that the presence of the overhead cirrus impacts both the AERI-retrieved AOD and the effective radius, generally resulting in positive biases in both AOD and effective radius, with the effect being larger in the latter because these cirrus clouds were optically thin.

[28] The AERI-retrieved AOD results in Figure 7 illustrate that there were several episodes during this storm event, with significant increases in the AOD on 7 March at 1200 UTC, on 8 March starting at 1200 UTC, and again on the 9 March starting at 0330 UTC. The temporal evolution of the mineral AOD is much easier to characterize using the infrared retrievals, as the solar-based methods (Cimel and MFRSR) do not provide any information at night. The effective radius of the kaolinite component of the dust retrieved from the AERI observations was a maximum of nearly 3.4 μm during the first episode of dust over Niamey on 7 March, and then gradually decreased during the next several days. The number of relatively large particles on 7 March is supported by the fair agreement between the 0.5-μm AOD from the MFRSR and the 11-μm AOD from the AERI. However, the relative number of smaller particles in the atmosphere increases significantly during 8–10 March, as the MFRSR-derived AOD, which is sensitive to both the fine and coarse mode aerosol particles (see Figure 5), is significantly higher than the AERI-retrieved AOD.

4.2. Year-Long Analysis

[29] The Sahel region of Africa experiences a significant change in the meteorological and dust conditions depending on the location of the intertropical front (ITF) [e.g., *Mbourou et al.*, 1997]. When the ITF at its more southerly location, Niamey and the entire Sahel area experience dry and dusty conditions; however, when the ITF moves toward its northerly location the Sahel experiences monsoon conditions and is much moister with significant amounts of precipitation. Furthermore, the change in the ITF location changes the wind patterns over the Sahel [e.g., *Slingo et al.*,

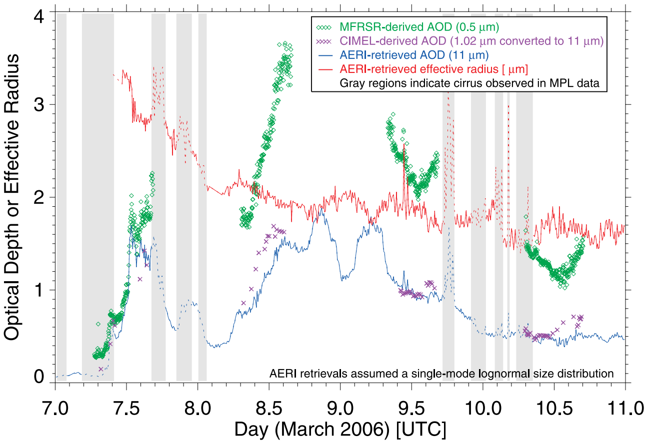

Figure 7. Time series of MIXCRA-retrieved 11-μm AOD (blue) and effective radius of the kaolinite component (red, micrometers) during the March 2006 dust storm. Vertical light gray bars indicate periods when thin cirrus were in the AERI's field-of-view as determined from ground-based lidar data. The AOD data show that there were several pulses of dust in this particular storm, whereas the effective radius of the kaolinite component show that the initial episode of dust had the largest dust particles (~3.5 μm) and that the effective size slowly decreased over the life of the storm. The visible (0.5 μm) AOD derived from the MFRSR are provided in green, as well as the 1.02-μm AOD from the Cimel, where the latter have been scaled to 11-μm AOD by multiplying by log(11.0 μm/1.020 μm).

2008]. Therefore, it is reasonable to expect changes in the AOD and composition associated with the location of the ITF.

[30] *Slingo et al.* [2008] have indicated that the onset of the monsoon in 2006 was not as dramatic over Niamey as is typically experienced at this location. Thus, we have elected to divide the year into 4 distinct periods: a premonsoon period when the ITF was south of the AMF site (from 7 January to 15 April), an early monsoon period that experienced the "false monsoon" (16 April to 3 July), a late-monsoon period when the ITF was well north of the AMF site (4 July to 28 October), and a postmonsoon period when the ITF moved well south of the AMF site again (29 October to 6 January).

[31] The time series of 11-μm AOD for the year is shown in Figure 8, with the four periods identified. The dust storm on 7–10 March is clearly the largest aerosol loading event, from an 11-μm point of view, during the entire year; however, there were significant aerosol loading events in the postmonsoon period as well as the early monsoon period. There are relatively fewer AOD retrievals during the two monsoon periods, especially the late-monsoon period, owing to the increased presence of clouds. The distributions of AOD for the four periods are shown in Figure 9. The AOD distribution is fairly similar for the premonsoon and postmonsoon periods, but the AODs are significantly smaller during the late-monsoon period.

[32] A natural question is: how accurate are the AERI-retrieved dust optical depths? To address this question, we compared the 11-μm AODs retrieved from the AERI with the 1.02-μm AODs derived from the Cimel sunphotometer (level 1.5) collected at Banizoumbou in clear-sky cases. A Cimel was installed at Niamey but was not operational until August 2006; thus we elected to use the larger data record at Banizoumbou for this comparison (Figure 10). The two data sets (Cimel from Banizoubou and MIXCRA) showed an excellent correlation (r = 0.913), with a linear relationship of Cimel_AOD (1.02 μm) = 2.175 × MIXCRA_AOD (11.0 μm) + 0.106 determined via simple linear regression (Figure 10a). Using the level 2 AERONET Cimel data from Banizoumbou in the comparison changes the statistics slightly, yielding a linear relationship of Cimel_AOD(1.02 μm) = 2.165 × MIXCRA_AOD(11.0 μm) + 0.121 and a correlation coefficient of 0.905, but the number of points available from level 2 is only 1026 versus 6033 using level 1.5 Cimel data. The Ångström exponent derived from the 1.02-μm Cimel AOD data and the 11-μm MIXCRA AOD retrievals is 0.526 ± 0.232, which is quite similar in both mean value and standard deviation to the Ångström exponent derived from the 0.675-μm and 1.020-μm Cimel AOD data (0.487 ± 0.215). However, while the mean values and the distribution (Figure 10c) of these two different Ångström values are similar, the correlation is poor (r = 0.095).

[33] As indicated above, a significant change in the wind direction is associated with the change in the location of the ITF. *Slingo et al.* [2008] show a substantial difference in the back-trajectories at 500 m (where the dust is assumed to reside) for the 4 different periods; the predominate back-trajectory direction is from the northwest-to-east during the premonsoon, rotating to the southwest with some notable events from other directions during the early monsoon period, to being predominantly from the south-to-southwest during the late-monsoon period, and then rotating back to a easterly direction during the postmonsoon periods. (Back-trajectories were computed with the HYPLIT model using analyses from the National Center for Environmental Prediction (NCEP) Global Data Assimilation System (GDAS).) Figure 11 shows the distribution of the daily averaged AERI-retrieved 11-μm AOD as a function of the back-trajectory direction, separated into octants, during the four periods. The gray diamonds are the actual daily averaged AOD values, with the number of samples in that octant listed directly below the octant's label. The filled black circle shows the median AOD value, with the black box showing the interquartile (25th to 75th percentile) spread and the vertical black bars showing the 5th to 95th percentile spread. Figure 11 illustrates, in a qualitative manner, the AOD's dependence on wind direction, as well as the relative fraction of time that the winds were from that direction.

[34] In the premonsoon period, the winds were primarily from the north, northeast, or east. The median AOT was larger when the winds were from the east than when the winds were from the north or northeast; while a few cases of significantly high AOD were noted when the winds were from the north or northeast, these few cases amounted to a small fraction of the total cases in those clusters. In the postmonsoon periods, the flow was either from the northeast or the east, but the median AODs were approximately the same; more frequent large AOD events were observed when the flow was from the east versus from the northeast. During the late-monsoon period, the flow was primarily from the southerly direction, and the median AOD was

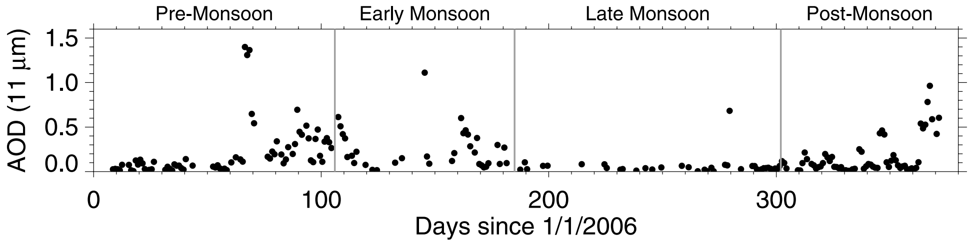

Figure 8. Daily averaged retrieved 11-μm AOD over the AMF during cloud-free AERI observations in 2006. There were significant aerosol loading events in each of the four periods; however, the largest AOD values occurred in the premonsoon and postmonsoon periods. The vertical gray bars separate the four periods and correspond to 15 April, 3 July, and 28 October.

quite small and had no significant dependence on wind direction. Interestingly, during the early monsoon period when the wind conditions were primarily from the south [see also *Slingo et al.*, 2008, Figure 9], the median AOD in the clusters when the flow was from other directions was relatively high. Because the surface is still relatively dry and bare (relative to the late-monsoon period), it seems that strong weather events associated with the onset of the monsoon are responsible for the lofting the dust in this early monsoon period. However, the number of samples in the different wind octants during the early monsoon period is small and thus pertains to a few distinct dust events.

[35] The radiatively significant aerosol composition for each successful cloud-free AERI sample was determined via an *F* test of the best single-mineral fit versus the best dual-mineral fit, as described above. Table 2 provides a breakdown of the number of cases that were classified as kaolinite-only, gypsum-only, quartz-only, kaolinite + gypsum, kaolinite + quartz, and quartz + gypsum for each of the four periods, as well as for the entire year. Kaolinite is an important component of the total mineral composition, with 94% of the retrievals during the year indicating that kaolinite (or minerals with similar refractive index spectra as kaolinite) was a significant component. This may have been suspected, since kaolinite has been shown to make up over 50% of the clay fraction of the soil particles with radius less than 1.5 μm in the Sahel region [*Hoose et al.*, 2008]. The most common mineral composition was a mixture of kaolinite+gypsum, with this combination considered the best in over 66% of the retrievals during the year. However, the fraction of cases where this mineral combination was considered the best was a function of period, which may imply a dependence on back-trajectory direction (i.e., origin of the air mass) although other factors may influence the mineral dust composition [e.g., *Sokolik and Toon*, 1999]. The fraction of cases where kaolinite + gypsum offered the best fit ranged from 19% of the time in the late-monsoon period to 75% of the time in the postmonsoon period. The mineral composition that fit the radiance observations the second best (after kaolinite + gypsum) was kaolinite-only dust, which was considered the best fit in 20% of the AERI retrievals. Interestingly, the fraction of cases where kaolinite + quartz offered the best fit was relatively constant at 7–8% in all periods, and the number of cases where the radiative composition was best described by only quartz or quartz + gypsum was almost negligible (0.3%).

[36] In all of the cases, single-mineral compositions were determined to yield the best fit statistically (as judged by the *F* test) approximately 25% of the time, and dual-mineral compositions yielding a better fit in the rest of the cases. The number of cases where single-mineral compositions were better than dual-mineral compositions were much larger in the two monsoon periods relative to the premonsoon and postmonsoon periods, with single-mineral fits determined to be better than dual-mineral fits 72% of the time in the late-monsoon period (Table 2). Cases that were determined to have single-mineral compositions typically had 11-μm AOD values below 0.1; however, over two thirds of all of the cases with AOD < 0.1 were determined to have dual-mineral compositions. The late monsoon was

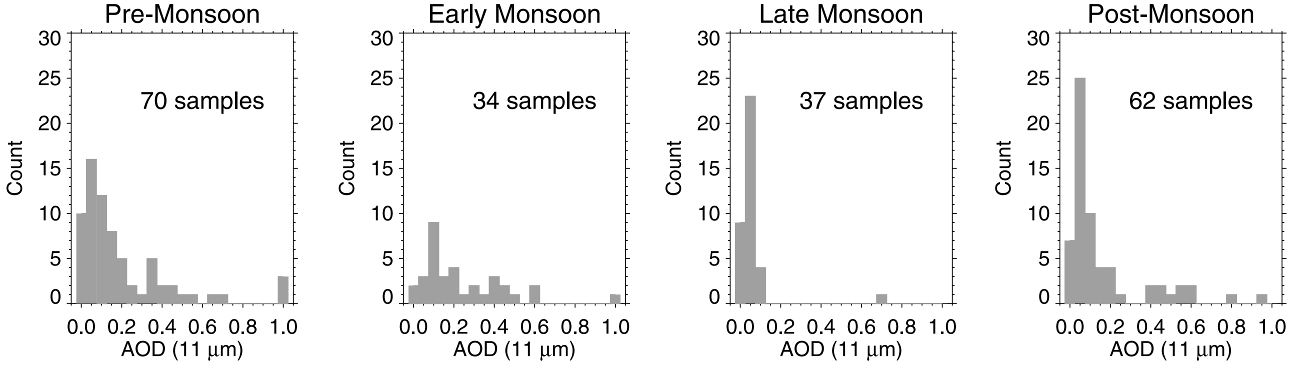

Figure 9. Distribution of daily averaged 11-μm AOD during each of the four periods. Samples with AOD > 1 are grouped together with the AOD = 1 bar in the histogram.

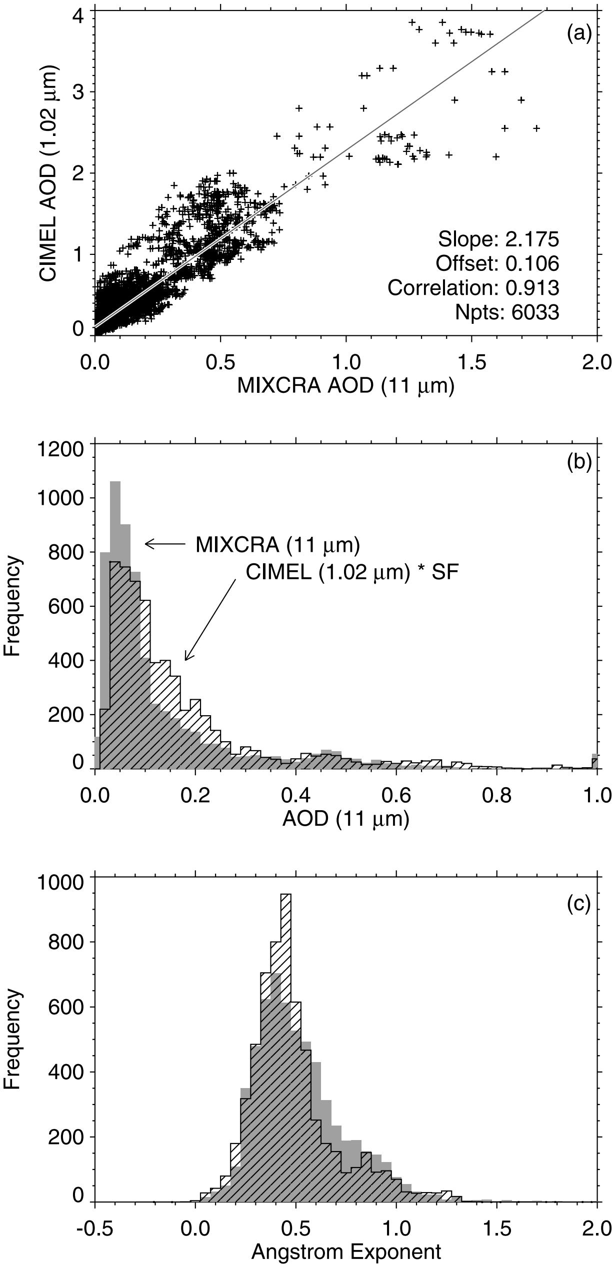

Figure 10. (a) Scatterplot of the AERI-retrieved 11-μm AOD versus the Banizoumbou Cimel sunphotometer 1.02-μm AOD. The Cimel data are level 1.5 from the AERONET data. (b) The distribution of 11-μm AOD from AERI (gray) and the Cimel (hashed), where the Cimel 1.02-μm AOD observations were multiplied by SF = log(11.0 μm/1.02 μm). (c) The distribution of Ångström exponent computed from 11-μm MIXCRA and 1.02-μm Cimel data (solid gray bars) and 1.02-μm and 0.675-μm Cimel data (hashed bars).

characterized by flow from the south, low dust aerosol optical depths (Figures 9 and 11), and significantly larger precipitable water vapor amounts than the premonsoon and postmonsoon periods [e.g., *Slingo et al.*, 2008]. As the PWV increases, the downwelling radiance is more heavily dominated by the water vapor emission (which increases by approximately the square of the PWV in the microwindows used in these retrievals). Thus, for larger PWV amounts, the uncertainty in the AOD retrieval increases, especially for cases with low amounts of aerosol, and the quality of the fit is decreased. *Nalli et al.* [2006] point out how fluctuations in PWV, especially when the PWV is large, can mask the signal from aerosol fluctuations; fortunately, the accurate water vapor retrievals from the MWR [*Turner et al.*, 2007] account for the majority of the fluctuations in water vapor. Nonetheless, the decrease in the quality of the fit when the PWV is large does not depend largely on the aerosol

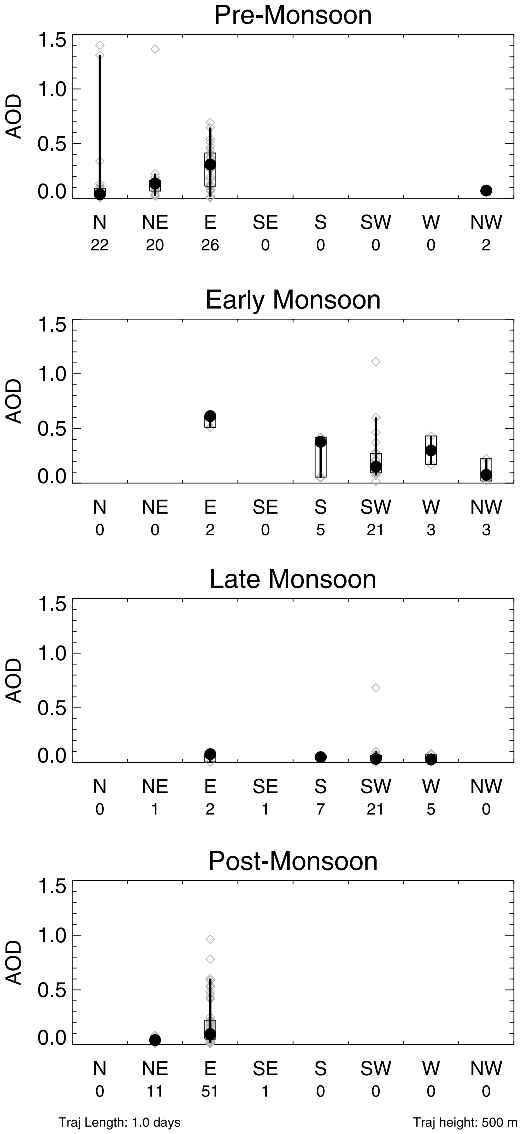

Figure 11. Distribution of daily averaged 11-μm AOD as a function of back-trajectory direction at 500 m for the four periods. The solid dot denotes the median, the open black rectangle illustrates the interquartile spread (most easily seen in the early monsoon period from the south direction), and the thin black bar denotes the 5th to 95th percentile spread. The number under each direction indicates the number of AERI samples included in that cluster. The gray points indicate the actual AOD values and thus illustrate the outliers in the distribution of AOD in each cluster. The data are not shown for clusters with less than two values.

Table 2. Best Fit Mineral Composition by Period[a]

Composition	Premonsoon	Early Monsoon	Late Monsoon	Postmonsoon	Entire Year
Kaolinite only	17.8%	29.9%	54.2%	13.7%	20.0%
Gypsum only	5.9%	4.1%	18.1%	4.0%	5.7%
Quartz only	0.0%	0.0%	0.0%	0.0%	0.0%
Kaolinite + Gypsum	68.7%	57.6%	19.0%	74.6%	66.6%
Kaolinite + Quartz	7.3%	8.2%	7.3%	7.5%	7.5%
Quartz + Gypsum	0.2%	0.1%	1.5%	0.1%	0.3%
Number of retrievals	5522	1999	1220	8014	16755

[a]The 16,755 valid retrievals are about 25% of the total number of AERI observations from 7 January 2006 to 6 January 2007; the other samples were excluded owing to clouds in the AERI field-of-view, the retrieval not converging, or if the retrieval was considered to have too much uncertainty in the retrieved variables.

composition, and thus the F test will tend to select the single-mineral fit as the "best fit composition" for cases with larger PWV, because the uncertainty in the computed radiance due to the uncertainty in PWV is larger when the PWV is large. This effect is observed in Table 2, where the frequency of single-mineral fits ranges from 24%, 34%, 72%, and 18% in the premonsoon, early monsoon, late-monsoon, and postmonsoon periods, respectively, where the PWV is largest during the late monsoon. Nonetheless, the single mineral fits during the late monsoon still indicate that kaolinite is the dominant mineral in the dust, with gypsum also an important component.

[37] Table 2 indicates that kaolinite and gypsum are the most common minerals in the dust above Niamey (from a radiatively significant point of view). Furthermore, we have seen that the four different periods are characterized by different back-trajectory directions, and thus a natural question is to see if the kaolinite fraction F_{kao}, defined above as the optical depth of the kaolinite to the total AOD, has a seasonal dependence. The distributions of F_{kao} for each of the four periods are shown in Figure 12 (gray) for the AERI observations that were best fit by the kaolinite + gypsum mineral composition. Both the premonsoon and postmonsoon periods exhibit a bimodal distribution of F_{kao} with peaks around 0.3 and 0.6; during the early monsoon period there is a third peak around 0.85. (There are relatively few kaolinite + gypsum retrievals during the late-monsoon period, and thus the statistics are not very good.)

[38] To investigate the dependence of F_{kao} with back-trajectory direction, the subset of retrievals associated with a back-trajectory from the easterly octant are indicated in black in Figure 12. Periods where the back-trajectories are from the east are characterized by smaller F_{kao} values (i.e., larger gypsum fractions F_{gyp}). Strong deflation events over the Bodélé depression (centered at approximately 17°N, 18°E) often result in large dust loadings that can have large concentrations of diatomite [*Washington et al.*, 2006b]. Diatomite is the fossilized remains of hard-shelled algae, and thus is found in ancient seabeds such as the Bodélé depression. Gypsum is a hydrated calcium sulfate that forms massive beds by precipitating out of highly saline water; thus gypsum may also be associated with the Bodélé depression. *Jacobson* [2001] concluded that gypsum was the most common solid-phase sulfate aerosol constituent in his global analysis of anthropogenic and natural aerosols. Furthermore, *Tegen et al.* [2006] have pointed out that the diatomite aerosols from the Bodélé depression are significantly different than the clay particles from the northern Sahara. The easterly back-trajectories over the AMF site cross over the Bodélé depression, and therefore it seems possible that the decrease in F_{kao} (increase in F_{gyp}) retrieved from the AERI observations is due to lofting and advection of mineral dust from this depression over Niamey. However, it is also possible that the gypsum over Niamey is the result of transport from much further away.

[39] MIXCRA also retrieves the effective radius (r_e) of the particles for both compositions, and thus the characteristic size of the dust particles can be investigated. Figure 13 shows the distribution of r_e for both kaolinite (top) and gypsum (bottom) from the kaolinite-only (solid gray) and kaolinite + gypsum (hashed) retrievals. Effective radii values are shown only if the uncertainty in the retrieved r_e is less than 60% of the uncertainty in the a priori r_e used in the optimal estimation retrieval (we assumed this uncertainty value to be 0.3 μm); retrievals that satisfy this constraint have enough information in the AERI spectrum to actually determine r_e, otherwise the retrieval tends to gravitate toward the assumed a priori r_e (0.8 μm for all three minerals). In general, the kaolinite particles have a smaller effective radius (between 1 and 3 μm) than the gypsum particles, which have effective radii between 3 and 5 μm. Diatomite particles from the Bodélé have been shown to be lofted from the surface in "flakes" [*Tegen et al.*, 2006], and the same may happen with possibly gypsum particles as well. The effective radius for the kaolinite in the kaolinite-only retrievals is slightly smaller than the effective radius of the kaolinite in the kaolinite + gypsum retrievals; this result may be due to a small amount of cross talk in the retrieval algorithm (especially at lower optical thickness when the aerosol signal is small).

5. Conclusions

[40] We have applied a retrieval method that derives the infrared AOD, effective radius, and the radiatively significant composition of mineral dust observed over Niamey, Niger, in 2006. These dust properties were retrieved from high-spectral-resolution infrared radiance data observed at the surface by the AERI instrument, one of the AMF instruments deployed during RADAGAST. The retrieval technique uses a physical retrieval to determine these dust properties, and propagates uncertainties in the radiative

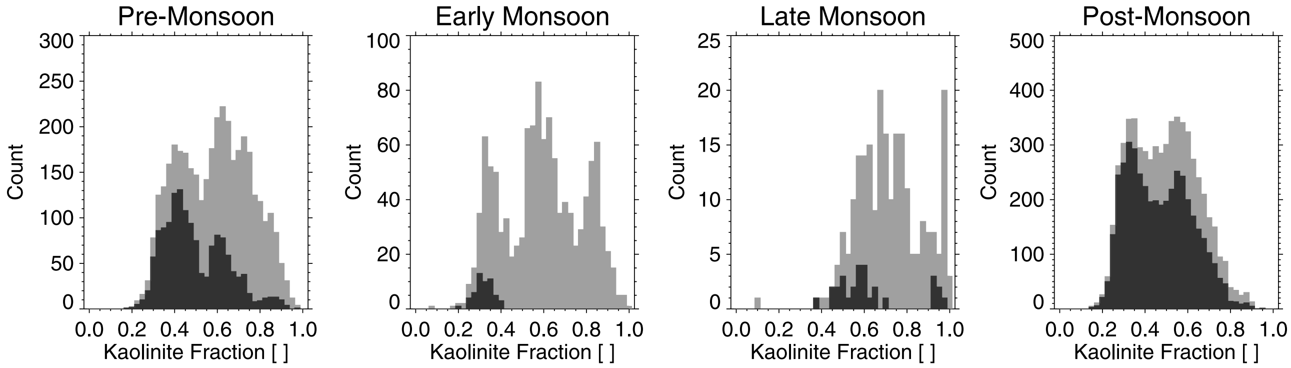

Figure 12. Distribution of kaolinite fraction, defined as $F_{kao} = \tau_{kao}/\tau_{tot}$, for each of the four periods (gray). The black histograms illustrate the subset of the data where the back-trajectories are from the eastern octant.

temperature of the dust layer, the amount of water vapor, and in the AERI radiance observations to provide uncertainties in the retrieved quantities. Three different minerals were used in the retrieval process (kaolinite, gypsum, and quartz), all of which have distinctively different absorption spectra in the thermal (8–13 μm) infrared. The retrieval algorithm was only run in cloud-free cases, yet over 16700 valid retrievals were made during the 1-year deployment.

[41] Comparisons with the yearlong data set of 11-μm dust AOD retrieved from the AERI with Cimel sunphotometer-derived optical depths at 1.02 μm showed a good linear correlation coefficient (r = 0.913). However, the AERI retrievals have a small positive bias in AOD relative to the CIMEL, even after a small warm bias is removed from the AERI radiance observations.

[42] When the year was separated into 4 distinct periods (premonsoon, early monsoon, late monsoon, and postmonsoon), the 11-μm AOD and radiatively significant composition show a dependence on season. The late-monsoon period has the lowest mean dust AOD, and the composition of the minerals was indicated to be kaolinite-only, kaolinite + gypsum, and gypsum-only in 54%, 19%, and 18% of the samples, respectively. The dust AOD was significantly larger in the premonsoon and postmonsoon periods, when kaolinite+gypsum was the most common composition (69% and 75% of the samples were this composition, respectively). The amount of gypsum in the kaolinite+gypsum retrievals is correlated with back-trajectory direction, with larger amounts of gypsum being retrieved when the back-trajectories cross the Bodélé depression region. The effective radius of the gypsum particles is significantly larger than the effective radius of the kaolinite particles (3–5 μm versus 1–3 μm, respectively). Interestingly, the results suggest

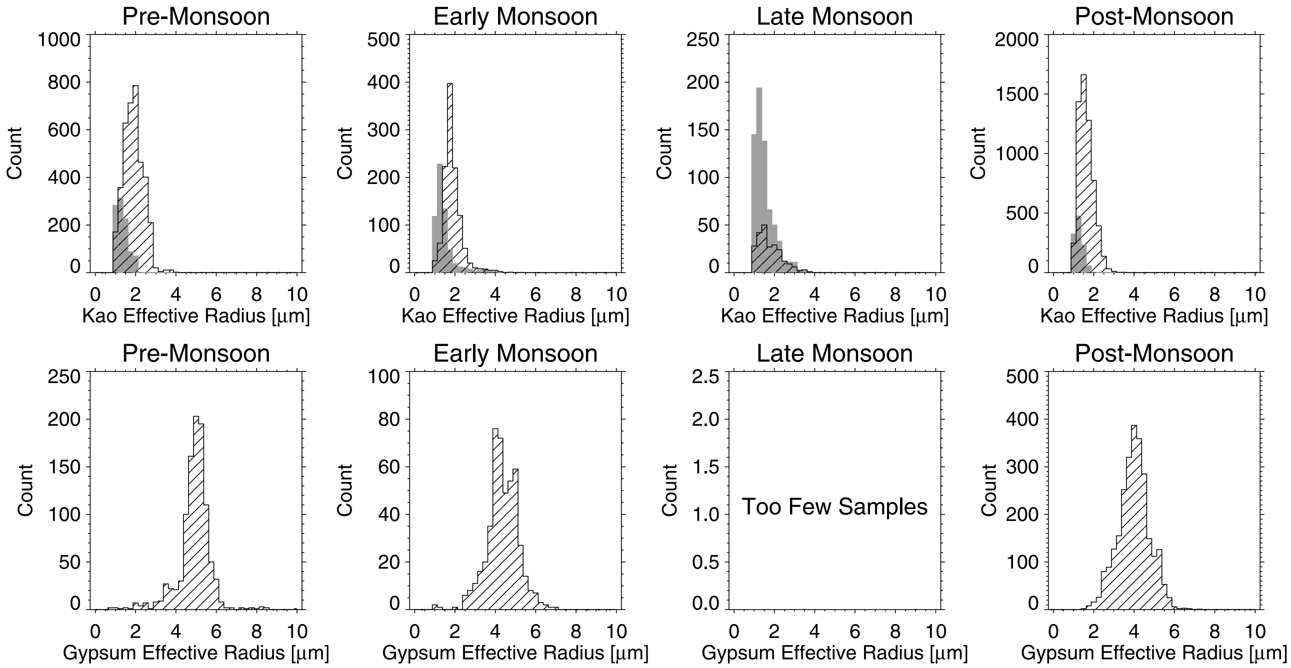

Figure 13. (top) Distribution of the effective radius of kaolinite for kaolinite-only (solid gray) and kaolinite + gypsum (hashed) retrievals, and (bottom) the distribution of effective radius for gypsum for kaolinite + gypsum retrievals in each of the four periods.

that quartz is a relatively insignificant mineral in the dust over Niamey.

[43] It is important to realize that the dust properties reported here are derived from the emission signature in the thermal infrared. One advantage of retrievals from infrared data is that the dust properties can be retrieved throughout the diurnal cycle. There is also little sensitivity to the composition of the aerosols in the fine mode of the size distribution, or to aerosols or minerals that do not have absorption bands in the 8- to 13-μm wavelength regime. This has both positive and negative aspects; for example, our technique is relatively insensitive to biomass burning aerosols as they tend to be fine-mode particles, and our technique also does not provide sensitivity to some of the minerals (such as hematite) found in the atmosphere. Hematite is an important component of the dust and is an important absorber of shortwave radiation in the visible wavelengths, but it does not have any absorption bands in the thermal infrared. Therefore, to fully characterize both the longwave and shortwave radiative impact of dust, the MIXCRA results must be combined with retrievals (e.g., the MFRSR technique by *Kassianov et al.* [2005]) that are sensitive to all of the radiatively significant minerals in the atmospheric dust.

[44] This effort provides a long-term, ground-based characterization of the mineral dust optical, physical, and chemical properties above the Sahel. These retrievals will be very useful in characterizing the radiative properties of the mineral dust over the site [e.g., *McFarlane et al.*, 2008], evaluating aerosol transport models [e.g., *Kinne et al.*, 2003], and for validation of satellite retrievals of dust optical depth over relatively bright surfaces.

[45] **Acknowledgments.** This project was funded by the U.S. Department of Energy, Office of Science, Office of Biological and Environmental Research, Environmental Sciences Division as part of the ARM program under grant DE-FG02-06ER64167. The AMF was deployed to Niamey as part of RADAGAST, which was proposed and organized by Tony Slingo; Tony has passed recently and his energy, enthusiasm, and scientific vision will be sorely missed. We would like to thank the AMF lead scientist Mark Miller and everyone associated with this experiment for the excellent data set that was collected. We would like to thank Ted Roush for the refractive index spectra, Sarah Bedka for helping to manually screen the data set for clouds, and Rick Wagener for the back-trajectory calculations. Evgueni Kassianov supplied the MFRSR AOD retrievals used here. The Cimel data were downloaded from the AERONET website (http://aeronet.gsfc.nasa.gov), and we thank Didier Tanré for answering questions regarding these data.

References

Aronson, J. R., A. G. Emslie, E. V. Miseo, E. M. Smith, and P. F. Strong (1983), Optical constants of monoclinic anisotropic crystals: Gypsum, *Appl. Opt.*, *22*, 4093–4098.

Cady-Pereira, K. E., M. W. Shephard, D. D. Turner, E. J. Mlawer, S. A. Clough, and T. J. Wagner (2008), Improved daytime column-integrated precipitable water vapor from Vaisala radiosonde humidity sensors, *J. Atmos. Oceanic Technol.*, *25*, 873–883, doi:10.1175/2007JTECHA1027.1.

Dubovik, O., A. Smirnov, B. N. Holben, M. D. King, Y. J. Kaufman, T. F. Eck, and I. Slutsker (2000), Accuracy assessments of aerosol optical properties retrieved from Aerosol Robotic Network (AERONET) Sun and sky radiance measurements, *J. Geophys. Res.*, *105*(D8), 9791–9806, doi:10.1029/2000JD900040.

Dubovik, O., et al. (2002), Variability of absorption and optical properties of key aerosol types observed in worldwide locations, *J. Atmos. Sci.*, *59*, 590–608, doi:10.1175/1520-0469(2002)059<0590:VOAAOP>2.0.CO;2.

Dufresne, J.-L., C. Gautier, P. Ricchiazzi, and Y. Fouquart (2002), Longwave scattering effects of mineral aerosols, *J. Atmos. Sci.*, *59*, 1959–1966, doi:10.1175/1520-0469(2002)059<1959:LSEOMA>2.0.CO;2.

Falkovich, A. H., E. Ganor, Z. Levin, P. Formenti, and Y. Rudich (2001), Chemical and mineralogical analysis of individual mineral dust particles, *J. Geophys. Res.*, *106*(D16), 18,029–18,036, doi:10.1029/2000JD900430.

Holben, B. N., et al. (1998), AERONET—A federated instrument network and data archive for aerosol characterization, *Remote Sens. Environ.*, *66*, 1–16, doi:10.1016/S0034-4257(98)00031-5.

Hoose, C., U. Lohmann, R. Erdin, and I. Tegen (2008), The global influence of dust mineralogical composition on heterogeneous ice nucleation in mixed-phase clouds, *Environ. Res. Lett.*, *3*, 025003, doi:10.1088/1748-9326/3/2/025003.

Intergovernmental Panel on Climate Change (2001), *Climate Change 2001: The Scientific Basis: Contribution of Working Group I to the Third Assessment Report of the Intergovernmental Panel on Climate Change*, edited by J. T. Houghton et al., 881 pp., Cambridge Univ. Press, New York.

Jacobson, M. Z. (2001), Global direct radiative forcing due to multicomponent anthropogenic and natural aerosols, *J. Geophys. Res.*, *106*(D2), 1551–1568, doi:10.1029/2000JD900514.

Kalashnikova, O. V., R. Kahn, I. N. Sokolik, and W.-H. Li (2005), Ability of multiangle remote sensing observations to identify and distinguish mineral dust types: Optical models and retrievals of optically thick plumes, *J. Geophys. Res.*, *110*, D18S14, doi:10.1029/2004JD004550.

Kassianov, E. I., J. C. Barnard, and T. P. Ackerman (2005), Retrieval of aerosol microphysical properties using surface MultiFilter Rotating Shadowband Radiometer (MFRSR) data: Modeling and observations, *J. Geophys. Res.*, *110*, D09201, doi:10.1029/2004JD005337.

Kinne, S., et al. (2003), Monthly averages of aerosol properties: A global comparison among models, satellite data, and AERONET ground data, *J. Geophys. Res.*, *108*(D20), 4634, doi:10.1029/2001JD001253.

Knuteson, R. O., et al. (2004a), Atmospheric Emitted Radiance Interferometer. Part I: Instrument design, *J. Atmos. Oceanic Technol.*, *21*, 1763–1776, doi:10.1175/JTECH-1662.1.

Knuteson, R. O., et al. (2004b), Atmospheric Emitted Radiance Interferometer. Part II: Instrument performance, *J. Atmos. Oceanic Technol.*, *21*, 1777–1789, doi:10.1175/JTECH-1663.1.

Koven, C. D., and I. Fung (2006), Inferring dust composition from wavelength-dependent absorption in Aerosol Robotic Network (AERONET) data, *J. Geophys. Res.*, *111*, D14205, doi:10.1029/2005JD006678.

Marra, A. C., A. Blanco, S. Fonti, A. Jurewicz, and V. Orofino (2005), Fine hemative particles of Martian interest: Absorption spectra and optical constants, *J. Phys. Conf. Ser.*, *6*, 132–138, doi:10.1088/1742-6596/6/1/013.

Mbourou, G., J. J. Bertrand, and S. E. Nicholson (1997), The diurnal and seasonal cycles of wind-borne dust over Africa north of the equator, *J. Appl. Meteorol.*, *36*, 868–882, doi:10.1175/1520-0450(1997)036<0868:TDASCO>2.0.CO;2.

McFarlane, S. A., E. I. Kassianov, J. Barnard, C. Flynn, and T. P. Ackerman (2008), Surface shortwave aerosol radiative forcing during the Atmospheric Radiation Measurement Mobile Facility deployment in Niamey, Niger, *J. Geophys. Res.*, doi:10.1029/2008JD010491, in press.

Miller, M. A., and A. Slingo (2007), The ARM mobile facility and its first international deployment: Measuring radiative flux divergence in West Africa, *Bull. Am. Meteorol. Soc.*, *88*, 1229–1244, doi:10.1175/BAMS-88-8-1229.

Nalli, N. R., et al. (2006), Ship-based measurements of infrared sensor validation during Aerosol and Ocean Science Expedition 2004, *J. Geophys. Res.*, *111*, D09S04, doi:10.1029/2005JD006385.

Rathke, C., J. Notholt, J. Fischer, and A. Herber (2002), Properties of coastal Antarctic aerosol from combined FTIR spectrometer and Sun photometer measurements, *Geophys. Res. Lett.*, *29*(23), 2131, doi:10.1029/2002GL015395.

Roush, T., J. Pollack, and J. Orenberg (1991), Derivation of midinfrared (5–25 μm) optical constants of some silicates and palagonite, *Icarus*, *94*, 191–208, doi:10.1016/0019-1035(91)90150-R.

Schuttlefield, J. D., D. Cox, and V. H. Grassian (2007), An investigation of water uptake on clay minerals using ATR-FTIR spectroscopy coupled with quartz crystal microbalance measurements, *J. Geophys. Res.*, *112*, D21303, doi:10.1029/2007JD008973.

Schwartz, S. E., and M. O. Andreae (1996), Uncertainty in climate change caused by aerosols, *Science*, *272*, 1121–1122, doi:10.1126/science.272.5265.1121.

Slingo, A., et al. (2006), Observations of the impact of a major Saharan dust storm on the atmospheric radiation balance, *Geophys. Res. Lett.*, *33*, L24817, doi:10.1029/2006GL027869.

Slingo, A., et al. (2008), Overview of observations from the RADAGAST experiment in Niamey, Niger: 1. Meteorology and thermodynamic variables, *J. Geophys. Res.*, *113*, D00E01, doi:10.1029/2008JD009909.

Sokolik, I. N., and O. B. Toon (1999), Incorporation of mineralogical composition into models of the radiative properties of mineral aerosol from UV to IR wavelengths, *J. Geophys. Res.*, *104*(D8), 9423–9444, doi:10.1029/1998JD200048.

Spitzer, W. G., and D. A. Kleinman (1961), Infrared lattice bands of quartz, *Phys. Rev.*, *121*, 1324–1335, doi:10.1103/PhysRev.121.1324.

Tegen, I., A. A. Lacis, and I. Fung (1996), The influence on climate forcing of mineral aerosols from disturbed soils, *Nature*, *380*, 419–422, doi:10.1038/380419a0.

Tegen, I., B. Heinold, M. Todd, J. Helmert, R. Washington, and O. Dubovik (2006), Modeling soil dust aerosol in the Bodélé depression during the BoDEx campaign, *Atmos. Chem. Phys.*, *6*, 4345–4359.

Turner, D. D. (2003), Microphysical properties of single and mixed-phase Arctic clouds derived from ground-based AERI observations, Ph.D. thesis, 167 pp., Univ. of Wisconsin-Madison, Madison. (Available from http://www.ssec.wisc.edu/library/turnerdissertation.pdf).

Turner, D. D. (2005), Arctic mixed-phase cloud properties from AERI-lidar observations: Algorithm and results from SHEBA, *J. Appl. Meteorol.*, *44*, 427–444, doi:10.1175/JAM2208.1.

Turner, D. D., B. M. Lesht, S. A. Clough, J. C. Liljegren, H. E. Revercomb, and D. C. Tobin (2003), Dry bias and variability in Vaisala radiosondes: The ARM experience, *J. Atmos. Oceanic Technol.*, *20*, 117–132, doi:10.1175/1520-0426(2003)020<0117:DBAVIV>2.0.CO;2.

Turner, D. D., D. C. Tobin, S. A. Clough, P. D. Brown, R. G. Ellingson, E. J. Mlawer, R. O. Knuteson, T. R. Shippert, and W. L. Smith (2004), The QME AERI LBLRTM: A closure experiment for downwelling high spectral resolution infrared radiance, *J. Atmos. Sci.*, *61*, 2657–2675, doi:10.1175/JAS3300.1.

Turner, D. D., S. A. Clough, J. C. Liljegren, E. E. Clothiaux, K. Cady-Pereira, and K. L. Gaustad (2007), Retrieving precipitable water vapor and liquid water path from Atmospheric Radiation Measurement (ARM) program's microwave radiometers, *IEEE Trans. Geosci. Remote Sens.*, *45*, 3680–3690, doi:10.1109/TGRS.2007.903703.

Vogelmann, A. M., P. J. Flatau, M. Szczodrak, K. M. Markovicz, and P. J. Minnett (2003), Observations of large aerosol infrared forcing at the surface, *Geophys. Res. Lett.*, *30*(12), 1655, doi:10.1029/2002GL016829.

Vömel, H., H. Selkirk, L. Miloshevich, J. Valverde, J. Valdés, E. Kyrö, R. Kivi, W. Stolz, G. Peng, and J. A. Diaz (2007), Radiation dry bias of the Vaisala RS92 humidity sensor, *J. Atmos. Oceanic Technol.*, *24*, 953–963, doi:10.1175/JTECH2019.1.

Washington, R., M. C. Todd, S. Engelstaedter, S. Mbainayel, and F. Mitchell (2006a), Dust and the low-level circulation over the Bodélé Depression, Chad: Observations from BoDEx 2005, *J. Geophys. Res.*, *111*, D03201, doi:10.1029/2005JD006502.

Washington, R., et al. (2006b), Links between topography, wind, deflation, lakes, and dust: The case of the Bodélé Depression, Chad, *Geophys. Res. Lett.*, *33*, L09401, doi:10.1029/2006GL025827.

D. D. Turner, SSEC, University of Wisconsin-Madison, 1225 West Dayton Street, Madison, WI 53706, USA. (dturner@ssec.wisc.edu)